A synergetic cocatalyst for conversion of carbon dioxide, sunlight and water into methanol

Zetian Mi (✉ ztmi@umich.edu)

 University of Michigan-Ann Arbor   https://orcid.org/0000-0001-9494-7390

Victor Batista (✉ victor.batista@yale.edu)

 Yale University   https://orcid.org/0000-0002-3262-1237

Zhengwei Ye (✉ zwye@umich.edu)

 University of Michigan

Ke Yang (✉ ke.yang@yale.edu)

 Yale University   https://orcid.org/0000-0003-0028-2717

Peng Zhou (✉ dpzhou@umich.edu)

 University of Michigan-Ann Arbor   https://orcid.org/0000-0001-8034-8282

Ishtiaque Navid (✉ inavid@umich.edu)

 University of Michigan

Yixin Xiao (✉ yxxiao@umich.edu)

 University of Michigan   https://orcid.org/0000-0001-6304-4092

Alexandre Pofelska (✉ pofelska@mcmaster.ca)

 McMaster University

Gianluigi Botton (✉ gbotton@mcmaster.ca)

 McMaster University   https://orcid.org/0000-0002-8746-1146

Tao Ma (✉ taoma@umich.edu)

 Michigan Center for Materials Characterization, University of Michigan

Shubham Mondal (✉ shbm@umich.edu)

 University of Michigan

Physical Sciences - Article

Keywords:

Additional Declarations: There is **NO** Competing Interest.

A synergetic cocatalyst for conversion of carbon dioxide, sunlight and water into methanol

Zhengwei Ye[1+], Ke Yang[2+], Peng Zhou[1], Ishtiaque Ahmed Navid[1], Yixin Xiao[1], Alexandre Pofelski[3], Gianluigi A Botton[3], Tao Ma[4], Shubham Mondal[1], Victor S. Batista[2*], and Zetian Mi[1*]

[1] Department of Electrical Engineering and Computer Science, University of Michigan, Ann Arbor, 1301 Beal Avenue, Ann Arbor, MI 48109, USA.

[2] Department of Chemistry, Quantum Institute & Energy Sciences Institute, Yale University, New Haven, CT 06520, USA.

[3] Department of Material Science and Engineering, Canadian Center for Electron Microscopy, McMaster University, 1280 Main Street West, Hamilton, ON L8S 4M1, Canada.

[4] Michigan center for materials characterization, University of Michigan, 2800 Plymouth Rd, Ann Arbor, MI 48109, USA

[+] These authors contributed equally to this work.

*E-mail: victor.batista@yale.edu; ztmi@umich.edu

The conversion of CO_2 into liquid fuels, using only sunlight and water, offers a promising path to carbon neutrality. An outstanding challenge is to achieve high efficiency and product selectivity. Here, we introduce a wireless photocatalytic architecture for conversion of CO_2 and water into methanol and oxygen. The catalytic material consists of semiconducting nanowires decorated with core-shell nanoparticles, with a copper-rhodium core and a chromium oxide shell. The Rh/CrOOH interface provides a unidirectional channel for proton reduction, enabling hydrogen spillover at the core-shell interface, as shown by density functional theory. The vectorial transfer of protons, electrons, and hydrogen atoms allows for switching the mechanism of CO_2 reduction from a proton-coupled electron transfer pathway in aqueous solution to hydrogenation of CO_2 with a record high solar-to-methanol efficiency of 0.29%. The reported findings demonstrate a highly efficient, stable, and scalable wireless system for synthesis of methanol from CO_2 that could provide a viable path towards carbon neutrality and environmental sustainability.

Solar-light conversion of CO_2 into liquid fuels such as methanol and ethanol can provide a viable solution to renewable energy production and mitigation of greenhouse gases.[1,2,3] To date, current strategies for CO_2 conversion rely mainly on thermocatalysis[4] and electrocatalysis[5] that consume a significant amount of thermal energy, or electricity. Solar light photocatalysis can offer a more sustainable approach.[6] The main outstanding challenges are to achieve: (1) high-efficiency of CO_2 reduction, and (2) high product selectivity toward liquid fuels. Semiconductor materials with a large band gap can provide energetic carriers to reduce CO_2, however, they unavoidably suffered from the limited light response range.[7,8] Furthermore, CO_2 reduction toward CO is often more favorable than toward liquid fuels.[9] Recently, theoretical and experimental studies have suggested the importance of intermediates with different binding modes in controlling the efficiency, selectivity, and reaction rates during CO_2 reduction. In fact, it has been suggested that *COOH is a key intermediate in the formation of CO and following hydrocarbon products, while HCOO* is a key intermediate in the formation of HCOOH.[10,11] Therefore, tuning the relative stability of reaction intermediates can favor a specific pathway and improve product selectivity during CO_2 reduction. Here, we show that selective formation of methanol can be enhanced by loading a bimetallic cocatalyst on a semiconductor photocatalyst.

In nature, metalloenzymes like the photosynthetic ribulose bisphosphate carboxylase (RuBisCO) and formate dehydrogenases of methylotrophic yeast and bacteria can reduce CO_2 with high selectivity toward specific products. For example, Mo- and W-dependent formate dehydrogenases (FDH) can reversibly catalyze CO_2 reduction to formate (**Scheme 1a**).[12-20] Inspired by enzymatic CO_2 reduction, we have developed a wireless architecture for selective CO_2 reduction reaction to methanol. The photocatalytic system consists of InGaN/GaN nanowires loaded with co-catalytic Cu-Rh/CrO_x core-shell nanoparticles (**Scheme 1b**), with bimetallic copper-rhodium cores and chromium oxide shells. Unique to this artificial photosynthetic system is the vectorial transfer of protons, electrons, and hydrogen atoms to Cu active sites, that can switch the mechanism from CO_2 reduction by conventional proton-coupled electron transfer (PCET) via *COOH in aqueous solutions to hydrogenation of CO_2 via HCOO*. High CO_2 reduction activity is shown under visible light irradiation in a mild environment (1 atm CO_2 atmosphere and pH 7 deionized water). Methanol is the major product, cogenerated with the dioxygen by-product in a 2:3 ratio. The system exhibits an average turnover frequency of 37.8 $\mu mol \cdot cm^{-2} \cdot h^{-1}$, with the best measured activity being 49.8 $\mu mol \cdot cm^{-2} \cdot h^{-1}$ (298.5 $mmol \cdot g^{-1} \cdot h^{-1}$), which corresponds to a record-high solar-to-liquid fuel efficiency of 0.29% and 0.38%, respectively.

Design Principles

InGaN/GaN nanowires function as visible-light absorbers by separating charge carriers (**Scheme 1b**). The photogenerated electrons flow into the Cu-Rh/CrO_x nanoparticles where protons are reduced and bind to the Rh surface as hydrogen atom adsorbates. Rh/CrO_x core-shell nanoparticles are known to be efficient catalysts for H_2 evolution by H_2O reduction.[21-23] On our Cu-Rh/CrO_x nanoparticles, the *in situ* generated hydrogen atoms spillover to the nearby Cu sites and react with CO_2. Here, CO_2 is hydrogenated leading to the selective production of CH_3OH, in contrast to electrocatalytic CO_2 reduction on Cu surfaces that typically yield a mixture of products.[24-32]

We synthesized interfacial structures of GaN/Rh, GaN/Cu, Rh/Cu, Rh/CrOOH, and Cu/CrOOH to explore the possibility of forming an efficient photochemical architecture (**Fig. 1a**), considering that electrons transfer from Cu to Rh since the work function of Rh is larger than that of Cu.[33] We found that the Rh(111) facet matches the GaN($10\bar{1}0$) facet very well, with a lattice mismatch < 4% (**Fig. 1b** and **Table S4**). The interaction between Cu and GaN, however, is not as favorable due to the larger lattice mismatch between the Cu(111) and GaN($10\bar{1}0$) surfaces (**Table S4**), yielding a weaker interaction (**Supplementary Figure 11**) and a large kinetic barrier for electron transfer from GaN to Cu. So, the electron transfer pathway from GaN to Rh determines the main electron transfer pathway since it is favored by both thermodynamics and kinetics.

Our density functional theory (DFT) analysis of Rh/CrOOH and Cu/CrOOH interfaces (**Fig. 1c** and **Supplementary Figure 12**) shows that Rh is likely covered by a CrOOH shell, as suggested previously by Domen and coworkers.[33] Furthermore, we find that the CrOOH shell is unlikely to form on Cu due to the lattice mismatch (**Table S5**) which prevents growth of CrOOH on Cu(111) (**Supplementary Figure 6, Supplementary Figure 9 and Supplementary Figure 12**). The Rh/Cr and Rh/Cu interfaces allow for unidirectional proton transfer and reduction, followed by hydrogen spillover from Rh to Cu. The exposed Cu surface enables hydrogenation of CO_2 by hydrogen adsorbates effectively inducing catalytic CO_2 reduction. Therefore, our DFT computational analysis supports the viability of the catalytic architecture shown in **Scheme 1b**.

We analyzed CO_2 reduction on Cu(111). We found that CO_2 reduction can occur via two reaction pathways, including standard electrochemical reduction by proton-coupled electron transfer (PCET) using electrons from the electrode and protons from the bulk solution, and hydrogenation by surface adsorbed H atoms (reducing equivalents of $H^+ + e^-$). We modelled the reduction of CO_2 with electrons by preparing a negatively charged Cu surface which serves as a model of the electrified Cu electrode. We analyzed binding of CO_2 on the charged Cu surface. We found that binding of CO_2 through the oxygen atoms is unfavorable, resulting in physisorption of CO_2 with distances of ~3 Å from Cu to O in the CO_2 molecule (**Fig. 1d**). However, binding of CO_2 through C forms a $*COO^-$ species which can be readily protonated by protons from the bulk solution to form the $*COOH$ intermediate, leading to formation of $*CO$ and ultimately hydrocarbon products such as CH_4, C_2H_4, etc. In fact, that is the favored mechanism for most electrochemical CO_2 reductions on Cu electrodes which exhibits poor selectivity. In contrast, when CO_2 is reduced by H atoms on the Cu surface, both the $*COOH$ and $HCOO*$ binding modes of CO_2 are possible, with the $HCOO*$ binding mode being more favorable. (**Fig. 1d**). Therefore, the photochemical architecture shown in **Scheme 1b** with vectorial transfer of protons, electrons, and hydrogen atoms to the Cu active site can achieve high selectivity of CO_2 photoreduction to CH_3OH. In the following section, we demonstrate that such a catalytic architecture can be experimentally realized on InGaN nanowires.

Results

Synthesis and characterization of photocatalysts. Single crystalline Mg-doped p-type InGaN/GaN nanowire arrays were grown on a silicon wafer utilizing molecular beam epitaxy (see Methods). The ratio of indium and gallium of InGaN was determined by X-ray diffraction (see Methods). The band gap of the InGaN/GaN nanowires was located at ~525nm. Co-catalysts Rh, Cu and Cr_2O_3 were then photo-deposited on the nanowire surface (see Methods). **Fig. 2a** shows InGaN/GaN nanowires grown on the silicon wafer with

an average length of ~1 μm and width of ~100 nm. **Fig. 2b** shows the high angle annular dark field-scanning transmission electron microscopy (HAADF-STEM) image of an InGaN/GaN nanowire after photo-deposition of co-catalysts (see Methods). The grey spots show that the co-catalytic nanoparticles decorated well the sidewalls of the InGaN/GaN nanowire. **Fig. 2e** shows the energy dispersive X-ray (EDS) elemental mapping of the material, showing 10 nm particles with a distinct Rh and Cu core and Cr_2O_3 shell. Note here that EDS mapping merely exhibits a 2-dimensional perspective, while the signals lay on the images with a 3-dimensional depth. Likewise, **Fig. 2c** shows the deposited core-shell particles of Rh, Cu and CrOOH ($Cr_2O_3 \cdot H_2O$) widely dispersed on the nanowire surface, also shown in **Fig. 2b**. Typically, the CrOOH shell shares a thickness of around 2 nm for most of the observed particles, corresponding to 3-4 layers of CrOOH (**Supplementary Figure 12**). The core could vary from 2 to 20 nm due to the randomness in the photo-deposition. As predicted by our DFT calculations (**Fig. 2d** and **Supplementary Figure 12**), $Cr_2O_3 \cdot H_2O$ self-assembles during the reaction *in-situ* and forms a film of CrOOH on the Rh surface.[33]

The average loaded amount of Rh, Cu and Cr is 0.067 μmol/cm^2, 0.21μmol/cm^2 and 0.0062 μmol/cm^2, respectively, estimated through inductively coupled plasma-atomic emission spectroscopy (ICP-AES). The chemical states of each photo-deposited cocatalyst were analyzed by X-ray photoelectron spectroscopy (XPS) before and after the photocatalytic reaction. The Rh $3d_{5/2}$ spectrum exhibits four peaks which correspond to the metallic and the oxidized state of Rh (**Fig. 2f**) indicating a strong interaction between Rh and CrO_x. It is further noticed that the ratio of intensities between the oxide and metal peaks increases after the photocatalytic reaction. **Fig. 2g** shows the Cu $2p_{3/2}$ XPS spectra taken before and after the photocatalysis reaction. Together with the location of copper LMM peak (**Supplementary Figure 2**) at 918.69 eV (Kinetic energy), these results show no chemical shift relative to metallic copper, suggesting a negligible amount of Cu_2O. Therefore, there is no significant interaction, or synergetic effect between chromium oxide and copper likely due to the lattice mismatch and weaker interactions between Cu and CrOOH. It is further noticed that both copper and chromium show no chemical shift before and after the reaction (**Fig. 2g, Fig 2h**). The XPS spectrum is thus consistent with our DFT calculations (**Fig. 2d**) showing that Rh atoms on the surface are directly interacting with both Cu atoms and CrOOH layers, while Cu atoms have no significant interaction with CrOOH. The Cu surface is thus exposed to the solution favoring adsorption of CO_2.

Photocatalytic reaction experiments and results. The photocatalytic performance of $RhCuCr_2O_3$/InGaN was characterized using a solar simulator, with water and CO_2 as the feedstocks (see Methods). Therefore, sunlight was the only energy input to this wireless photocatalytic reaction. **Figure 3a** shows the rate of generation of CH_3OH, H_2, CH_4, and O_2 using InGaN with (or without) the incorporation of Cu and Rh/CrOOH co-catalysts, averaged over three cycles (see Methods). We find that InGaN nanowires exhibit a negligible photocatalytic activity. Incorporation of Rh/CrOOH enhances the photocatalytic activity, yielding H_2 and O_2 as the major products due to water splitting, as well as trace amounts of CH_3OH. Incorporation of Cu on the InGaN nanowire arrays generates a small amount of CH_3OH and trace amounts of CH_4 and O_2. InGaN nanowires with both Cu and Rh/CrOOH exhibit a dramatic enhancement in the production rate and selectivity for CH_3OH. Generation of CH_3OH and O_2 maintains a stoichiometric ratio of 2:3 only when loading both Cu and Rh/CrOOH.

The analysis of the photocatalytic performance of InGaN nanowire arrays with either Rh/Cu or Cu/CrOOH provided further insights on the reaction mechanisms and confirmed the superior performance of the

Rh/Cu/CrOOH@GaInN photocatalysts. **Fig. 3a** shows the performance of Rh/Cu and Cr/Cu deposited on InGaN nanowires. Significant loss of catalytic activity is observed for InGaN nanowires with only Rh/Cu without CrOOH, or only Cu/CrOOH without Rh. Those results show that the highest turnover frequency and selectivity of methanol generation is obtained when Rh, Cu, and CrOOH are simultaneously incorporated into the InGaN nanowires. The simultaneous incorporation of Rh, Cu and CrOOH also leads to high turnover numbers with stable production of methanol over many cycles.

An important observation is that CrOOH does not function as a protective shell to preserve the methanol production efficiency in the case of Cu/CrOOH, even though it significantly enhances the overall water splitting performance in the case of Rh/CrOOH. These differences are likely due to the lattice mismatch between CrOOH (2.98 Å) and copper (2.56 Å), which prevents formation of the Cu/CrOOH core-shell structures observed for Rh with CrOOH (**Supplementary Figure 12**). In fact, significant differences in composition of the surface were confirmed by STEM characterization and the EDS signals spectrum of Cu/CrOOH of co-deposited samples (**Supplementary Figure 6**). Our data thus provides unambiguous evidence for a synergistic effect of Rh, Cu, and CrOOH in promoting CO_2 reduction to methanol. Significantly, the production of methanol and oxygen remains nearly stoichiometric when using the Rh/Cu/CrOOH@GaInN photocatalysts. The activity of methanol and oxygen production remains nearly constant during three cycles of measurements (**Fig. 3c)**, showing negligible decomposition or poisoning of the photocatalyst, commonly reported for other systems developed for photo-driven CO_2 reduction.

Next, we have studied the effect of different loading amounts of Cu and Rh on the photocatalytic performance for reduction of CO_2 to CH_3OH (see Methods). **Fig. 3b** shows that a relatively low rate of CH_3OH and low selectivity is observed when either Rh, or Cu dominates, presumably due to the lack of proper formation of Rh/CrOOH/Cu core-shell structures under those extreme deposition conditions. In addition, we observe a high production rate (49.7 $\mu mol \cdot cm^{-2} \cdot h^{-1}$) and high selectivity (>80%) for a wide range of Rh/Cu precursor ratios (*e.g.,* from 10:2 to 2:10), consistent with formation of robust Rh/CrOOH/Cu core-shell structures as confirmed by STEM characterization.

Our analysis of products source tracing and GC/NMR measurements utilizing $^{13}CO_2$ and $H_2^{18}O$ as feedstocks (see Methods) confirms that C in the product CH_3OH originated from carbon dioxide. Furthermore, our analysis of the gas products from gas chromatography-mass spectrometry (GC-MS) (**Fig. 3d**) shows a clear m/z = 36 peak due to $^{18}O_2$, confirming that the by-product dioxygen was generated from water, consistent with the reaction mechanism predicted by our DFT calculations. Furthermore, our analysis of the liquid products by nuclear magnetic resonance (NMR) (**Fig. 3e**) shows a clear split peak due to the extra neutron in ^{13}C atom, supporting that $^{13}CO_2$ is the C source of methanol.

The change of attenuated total reflectance (ATR) signals at $CO_2/H_2O/RCC@GaInN$ interface reveals the gain or loss of species. As shown in **Fig. 4a**, during 60 min irradiation, the IR negative peak at 2355 cm^{-1}, attributed to the antisymmetric stretching vibration of O=C=O in CO_2,[34] sharply decreased with irradiation time due to CO_2 reduction. Meanwhile, an increasing IR peak at 1198 cm^{-2}, attributed to the stretching vibration of C–O bond in C–O–H, was also observed, which was close to the reported C–OH stretching band on Cu,[35] further demonstrating the reduction of CO_2.

We have further performed long-term stability studies of the Rh/Cu/CrOOH@InGaN photocatalysts. The measurements for the stability test were performed on separately prepared samples for a total of twelve cycles (**Fig. 4b)** (see Methods). The results show a decrease in performance along the evolution of multi-cycles,

although the productivity remained at a fairly high level >15 $\mu mol \cdot cm^{-2} \cdot h^{-1}$. The activity loss is not due to degradation of the InGaN/GaN nanowire light absorber but rather related to mechanical loss of coated metal particles during rinsing, as confirmed by a detailed STEM characterization of the nanowire after the reaction (**Fig. 4c**). Between each cycle of the reaction, the sample was rinsed with deionized water to remove traces of methanol that might otherwise affect the analysis of performance. The rinsing process, however, unavoidably removed some number of co-catalysts and nanowires from the surface. In fact, the loadings of both Rh and Cu were significantly reduced by rinsing as characterized by ICP-AES. In future studies, we will explore enhancing the mechanical stability of the catalyst by coating the surface of the co-catalyst nanoparticles with a thin layer of Al_2O_3 or TiO_2.

Studies of reaction mechanisms. Our computational analysis of CO_2 reduction on the Cu(111) surface has been performed at the DFT level. The work functions of Cu and Rh and the favorable contact between Rh(111) and GaN(10$\bar{1}$0) surfaces, favors a mechanism where photoelectrons transfer to the Rh nanoparticles and reduce protons on the Rh surface to form surface bound hydrogen atoms. Once the hydrogen atom adsorbates saturate the coverage of the Rh(111) surface, they diffuse to nearby Cu surface sites since the diffusion barriers for hydrogen atoms on transition metal surfaces are small (~ 0.1 eV).[34]

The calculated adsorption energy of hydrogen on bare Rh(111) and Cu(111) surfaces (i.e., at a low coverage of $\theta = 1/12$) is −0.64 and −0.34 eV, respectively (**Table S6**). The obtained binding energy on Rh(111) is in fairly good agreement with the experimental value (-0.80 eV) for low coverage of hydrogen on Rh(111),[35] while the calculated adsorption energy on Cu(111) is consistent with previously reported computational results of -0.3 to -0.4 eV on Cu(111).[34,36-37] Clearly, hydrogen adsorbs more strongly on bare Rh(111) than on Cu(111). However, in our photocatalytic system, the Rh(111) surface is covered by CrOOH. So, we have analyzed the adsorption energy of hydrogen at the Rh(111)/CrOOH(001) interface. Adding more CrOOH layers move the hydrogen adsorption energy at the Rh(111)/CrOOH(001) interface more positive, making the spillover of H from the Rh(111)/CrOOH(001) interface to Cu(111) energetically favorable (**Table S6**). As already demonstrated in previous experimental study,[33] the CrOOH shell allows selective permeation of protons from bulk solution to the Rh/CrOOH interface. The work function difference between Rh and Cu ensures the preferred transfer of photo-generated electrons to Rh, providing a unidirectional channel for proton reduction. Furthermore, the interface modulates the hydrogen adsorption energy on the Rh(111) surface, enabling spillover of hydrogen atoms generated *in situ* at the interface to nearby Cu sites. Hydrogen on Cu serves as a reductant for hydrogenation of CO_2 (**Fig. 5a**).

Fig. 1c (also see SI, **Supplementary Figure 13)** shows that the CrOOH shell on top of the Rh core allows for proton transfer from the bulk solution to the Rh(111) surface. At the same time, the CrOOH film prevents other species (*e.g.,* O_2) to approach the Ru(111) surfaces and consume the reductive H atoms generated *in situ*. The resulting design ensures effectiveness of the Rh/CrO$_x$ core-shell structure for photoreduction of protons.[33]

The surface H atoms generated *in situ* at the Rh(111)/CrOOH(001) interface can either generate H_2 or diffuse to the Cu surface to hydrogenate CO_2. The H spillover from the Rh/CrOOH interface to the Cu(111) surface is thermodynamically allowed (**Fig. 5a**). On the Cu surface, hydrogen atoms reduce CO_2 generating the formate intermediate bound to the surface through its O atoms (bi-HCOO*). As shown in **Fig. 1d**, the bi-HCOO* intermediate leads to high selectivity of CO_2 reduction to CH_3OH.

The Bader charge analysis (**Table S7**) suggests that the surface bound H atom is better described as a

hydride, as indicated by its negative charge, and is able to reduce CO_2 forming the negatively charged $HCOO^-$. There are two possible pathways to reduce the bi-HCOO* with a surface H atom. One pathway is the attack on the O site, resulting in the *HCOOH intermediate. The other pathway is hydride transfer to the C site, resulting in the *OCH_2O* intermediate. Previous studies of hydrogenation of CO_2 over Cu catalysts suggest that both pathways are possible at the gas/catalyst interface.[39-40] Here, we find that the free energy profiles for reduction of bi-HCOO* to *HCOOH and *OCH_2O* are indeed very similar without solvation (**Supplementary Figure 14**). Upon considering the solvation effect, however, *HCOOH is greatly stabilized (**Table S8**).

Fig. 5b shows that the pathway via *HCOOH is thermodynamically more favorable. It is noteworthy that the *OCH_2O* intermediate, which has been suggested to be an important intermediate in gas-phase CO_2 hydrogenation over Cu catalysts,[40] is similar to the *OCH_2O* intermediate observed upon CH_4 oxidation,[41] suggesting its central role in both CH_4 oxidation and CO_2 reduction in the gas phase. In aqueous CO_2 reduction, however, *OCH_2O* is not as important as HCOOH* due to its poor water solubility (**Table S8**).

Further reduction of the HCOOH* intermediate forms the *OCH_2OH* intermediate, which has been suggested to be important in CO_2 hydrogenation.[36-38] Further reduction of *OCH_2OH* can generate both *OCH_3 + *OH, or *$O=CH_2$ + *OH_2, where the former pathway is thermodynamically favored (**Fig. 5b**). The *OCH_3 intermediate can be further reduced to CH_3OH*, leaving the Cu surface to complete the catalytic cycle.

The mechanism shown in **Fig. 5** involves reduction of CO_2 by H atoms adsorbed on the Cu surface, a process equivalent to proton coupled electron transfer in electrochemical CO_2 reduction. H spillover from the Rh/CrOOH interface to the Cu surface is energetically favorable. The reduction of bi-dentate HCOO* to HCOOH* is a thermodynamically 'uphill' process, so the bi-dentate bound HCOO* should be a detectable intermediate by *in situ* spectroscopy. Reduction of CO_2 according to this mechanism thus involves hydrogenation by *in situ* generated H atom adsorbates, leading to high selectivity for CH_3OH production. Consistently, our experiments show CH_3OH production with no significant amounts of any kind of by-product (e.g., CO, HCOOH, H_2CO, or CH_4). Furthermore, no enhancement of CH_3OH production is observed in the presence of H_2 consistent with reducing equivalents being generated *in situ*.

It is important to compare our reaction mechanism, with an industrial process for CH_3OH production[39] based on hydrogenation of CO_2, catalyzed by metallic surfaces such as Cu(111), a process that requires *thermal* cleavage of the H–H bond at 500 K. In contrast, our catalytic system generates H atoms *in situ* at room temperature on the Rh/CrOOH surface, allowing for CO_2 reduction to CH_3OH under ambient temperature and pressure. **Fig. 5b** shows that upon formation of the HCOOH* intermediate, the subsequent reaction steps are quite favorable. Therefore, formation of HCOO* represents the mechanistic bottleneck of CO_2 reduction on the Cu surface, particularly during heterogeneous CO_2 hydrogenation in the gas phase (**Supplementary Figure 14**) due to the large free energy cost of generating *OCH_2O*, or *HCOOH intermediates. Therefore, it is unsurprising that the industrial production of methanol from mixtures of CO/CO_2/H_2 (synthesis gas) over a Cu/ZnO/Al_2O_3 catalyst requires typical reaction conditions of 230-280 °C and 50-120 atm.[39] Remarkably, we find that H atom adsorbates on Cu(111) can reduce CO_2 in aqueous solution, facilitating the conversion of HCOO* to HCOOH*, and thus making CH_3OH production possible under ambient temperature and pressure (**Supplementary Figure 15**). In addition, the overall reaction can be driven by the *in situ* generated H atoms at the Rh/CrOOH interface through H spillover (**Supplementary Figure 16**).

Discussion

We have introduced novel structures of photocatalytic systems that can switch the mechanism of CO_2 reduction from conventional PCET of electrocatalytic systems on Cu surfaces to hydrogenation of CO_2. For catalysts consisting of Rh/CrOOH and Cu, the dominant pathway is hydrogenation of CO_2 by *in situ* generated H adsorbates, leading to highly selective production of CH_3OH via the HCOO* intermediate. With only Cu serving as a cocatalyst for proton reduction, both pathways are open, including PCET via *COOH and hydrogenation of CO_2 via HCOO*, leading to low selectivity with production of both H_2, CH_3OH and CH_4. The PCET pathway becomes predominant for hydrocarbon generation when applying a sufficiently negative bias potential to the Cu electrode. However, the resulting reaction still exhibits poor selectivity.

It is important to compare the performance of our catalytic systems to the catalytic cofactors of natural enzymes that reduce CO_2 with high selectivity. For example, molybdoenzyme formate dehydrogenases[39] catalyze the reduction of CO_2 to formate, while carbon monoxide dehydrogenases reversibly reduce CO_2 to CO. Remarkably, these two types of enzymes catalyze the two alternative pathways of CO_2 reduction observed on Cu electrodes with catalytic nanowires, including hydrogenation of CO_2 via the HCOO* intermediate and the PCET through the *COOH reaction intermediate.

Fig. 6 shows the binding modes of CO_2 in the two enzymes, the relevant intermediates characterized by X-ray crystallography, as compared to the optimized CO_2-bound intermediate on the Cu (111) surface. The pathway leading to formation of CO in both CO dehydrogenases and the Cu surface involves the *COO⁻ intermediate. In contrast, the pathway leading to formation of formate involves HCOO*. The C–O bond lengths of *COO⁻ bound to the Cu(111) surface agree with those in the [Ni-Fe] CO dehydrogenase, where the CO_2 is bound at the active site with C and O coordinated to two nearby metal centers. While no CO_2-bound intermediate has been characterized by X-ray crystallography for formate dehydrogenases, a crystallographic model structure of the complex of formate dehydrogenase and nitrite is available,[40] providing insights on the binding mode of CO_2 in formate dehydrogenase since NO_2^- and $HCOO^-$ are isoelectronic.

Fig. 6e and **6f** show that intermediates with CO_2 bound to metal centers through O atoms in both the enzyme active sites and the Cu surface led to hydride transfer and formation of formate. The main difference when comparing the binding modes of NO_2^- and $HCOO^-$ is that NO_2^- (and presuming $HCOO^-$) binds to [Mo]-formate dehydrogenase as a mono-dentate O binding mode ligand, while $HCOO^-$ binds to the Cu(111) surface and exhibits a bi-dentate O binding motif. Beyond these small differences in binding modes, the comparison shows that the selectivity of CO_2 reduction for one or the other reaction pathway can be tuned by tuning the specific binding mode of CO_2 to the active site in either the catalytic cofactor in the natural enzyme or the synthetic catalysts. In our catalytic system, selectivity toward CH_3OH is achieved by introducing bi-metallic active sites that play specific functional roles during the photochemical CO_2 reduction.

PCET and hydrogen atom transfer are two different ways to deliver a reducing equivalent to CO_2 during the reduction reaction. Beyond CO_2 reduction, the PCET mechanism is ubiquitous in electrochemical, photoelectrochemical, and photochemical reactions in aqueous solutions. In contrast, hydrogen-atom transfer is more important in gas phase reactions, and in non-polar solutions. Our Rh/Cu/Cr system, however, operates in aqueous solutions and suppresses PCET on the Cu surface by enabling the unidirectional flow of photoelectrons from GaN to Rh. The shell of CrOOH allows for directional proton transfer from the bulk

solution to the Rh surfaces. The two directional processes enable the generation of reducing equivalents at the Rh/CrOOH interface leading to hydrogenation of CO_2 upon hydrogen spillover from Rh to Cu.

The use of two metals with different work functions is crucial for establishing directionality of electron transfer while CrOOH has OH groups between layers (**Supplementary Figure 13**) that enable effective proton translocation through a Grotthus-type mechanism, as commonly observed in biological systems.[41] The CrOOH film also serves as an effective membrane that allows proton transfer from the bulk solution to the electrode surface while blocking other species (e.g., O_2) that could compete with proton during the reduction reaction. Therefore, directional proton and electron transfer pathways in our Rh/Cu/Cr system mimic analogous directional processes for proton and electron transfer in enzymes (**Scheme 1**), providing a biomimetic system and inspiration for development of catalysts materials for selective chemical transformation.

Conclusion

We have shown that catalytic materials based on Rh/Cu/CrOOH nanoparticles dispersed on InGaN/GaN surfaces enable *in-situ* generation of hydrogen atoms on the Rh surface that spillover Cu where CO_2 is selectively reduced by hydrogenation to methanol with high production rate and selectivity. A record-high activity of 37.38 $\mu mol \cdot cm^{-2} \cdot h^{-1}$ and a maximum solar-to-fuel conversion efficiency of 0.29% is achieved. The reported results demonstrate an unrivaled artificial photocatalytic configuration for unitary production of methanol and hydrogen from visible light using CO_2 and water as the only chemical inputs.

Method

Synthesis of InGaN/GaN nanowires. InGaN/GaN nanowire arrays were grown on a silicon wafer using a plasma-assisted MBE system. The catalyst-free nanowire growth was carried out under a nitrogen-rich environment to promote formation of N-terminated surfaces protected against photo corrosion and oxidation. The nanowires, consisting of multiple segments of InGaN/GaN, were doped with a p-type magnesium dopant. Ga and In beam equivalent pressures (BEPs) were set at ~7.35×10^{-8} Torr and ~7×10^{-10} Torr, respectively, and the growth temperature of InGaN was ~765 °C.[21,22]

Cocatalyst loading. Rh, Cr_2O_3, and Cu co-catalyst nanoparticles were loaded on InGaN/GaN nanowires by photo deposition. The InGaN/GaN wafer was firstly stabilized on a Teflon holder. Then the holder was transferred to a reaction chamber containing 50 mL of 20vol% methanol aqueous solution. 5 μL of 0.2 mol L^{-1} Na_3RhCl_6 (Sigma-Aldrich), 5 μL of 0.2 mol L^{-1} K_2CrO_4 (Sigma-Aldrich), and 5 μL of 0.2 mol L^{-1} $CuCl_2 \cdot 2H_2O$ (Sigma-Aldrich) were added to the solution. The chamber was covered by a quartz cover and vacuumized. The chamber was irradiated under 300 W Xe lamp (Cermax, PE300BUV) for 30 min[23]. Finally, the obtained photocatalyst wafer was soaked in 70 °C deionized water under vacuum for 10min and dried at 80°C in vacuum.

Carbon dioxide reduction. The photo-reduction of CO_2 was performed in a glass chamber (diameter, 80mm; volume, 400 mL) sealed with a top quartz window under 300 W xenon lamp illumination. Both AM1.5G filter and 400nm long pass filters were inserted between the lamp and the reaction chamber. Prior to illumination, 50 mL of distilled water was purged with high-purity CO_2 (PurityPlus, 99.8%) for 15 minutes and then poured into the chamber. Subsequently, the chamber was vacuumized to further remove any gas in the water. The chamber was then filled with high-purity CO_2 (99.8%), and purged with CO_2 for 10 minutes. Before illumination, the chamber was placed in a water bath bed to stabilize the temperature. After 10 minutes, the lamp was mounted on the reaction chamber to start illumination. During the stability test, at an interval of 1 hour, the sample was taken out of the reaction chamber, exposed to air, rinsed with deionized water, and dried in CO_2 flow to get rid of the methanol adsorbed on the surface. The chamber was also thoroughly cleaned. The next cycle of the reaction was then conducted to test the device stability.

Characterization. Hydrogen and oxygen samples were examined by GC (Shimadzu GC-8A, TCD detector). Carbonate gas samples were examined by GC (Shimadzu GC-2010 Plus, FID detector), and the carbonate liquid samples were examined by GC (Shimadzu GC-2010 Plus, FID detector). The crystal structure of InGaN/GaN nanowires was examined by X-ray diffraction (XRD), which was collected on a Rigaku X-ray diffractometer equipped with Cu Kα radiation working at the accelerating voltage of 40 kV and the current of 80 mA. The morphology of sample was observed using a TESCAN MIRA's 4th generation Scanning Electron Microscope (SEM). The high-angle annular dark field scanning transmission electron microscopy (HAADF-STEM) analysis was performed on a FEI Titan Cubed 80–300 STEM operating at 300 keV with a current of approximately 80 pA. The Energy dispersive X-ray (EDS) elemental mapping was performed on a Thermo Fisher Talos F200X G2 S/TEM with a 200 kV accelerating voltage.

Products source tracing and GC/NMR measurement. $^{13}CO_2$ (99.0 atom %, Sigma-Aldrich) and $H_2^{18}O$ (97 atom %, Sigma-Aldrich) were used in tracing experiments to investigate and verify the molecular origin of oxygen and carbon during production of methanol and dioxygen. In the ^{13}C source tracing experiment, the samples were collected in a $^{13}CO_2$ atmosphere with samples placed in deionized water (~7 pH), illuminated with simulated AM1.5G sunlight, 400nm long pass filter filtrated 300W Xe lamp (light intensity is ~3.6W/cm^2). Samples were further examined by ^1H NMR (Varian Vnmrs 500) spectroscopy. In the ^{18}O source tracing experiments, the samples were collected in a CO_2 atmosphere with devices placed in 1ml $H_2^{18}O$ deionized water mixed with 9ml H_2O (~7 pH), illuminated with AM1.5G, 400nm long pass filter filtrated 300W Xe lamp (light intensity is ~3.6W/cm^2). Then, the gas sample was further examined by GC-MS (Shimadzu QP-2010 GC/MS, 30-meter-long DB-5 column with a 0.25 mm I.D., FID detector) to determine the ^{18}O.

***In-situ* ATR experiments.** *In-situ* attenuated total reflectance (ATR) experiments are conducted on FT-IR Spectrometer (Bruker) INVENIO. In the general procedure, nanowires samples were scratched off from the silicon wafer and sealed with DI water (pre-purged with CO_2) in the ATR chamber with a quartz window. The CO_2 was flown through the chamber until equilibrium and taken as a blank background. IR signals were *in-situ* collected during the incident irradiation of a 420 nm LED (3W) through the quartz glass window.

Calculation of solar-to-fuel (STF) efficiency. The STF efficiency for photocatalytic CO_2 reduction reaction was calculated, as follows:

$$STF = \frac{\text{Energy of generated } CH_3OH}{\text{Solar energy irriadiating the device}} = \frac{E_{CH_3OH}}{E_{solar}} \qquad (1)$$

The CO_2 RR to methanol is shown below,

$$2CO_2 + 4H_2O \rightarrow 2CH_3OH + 3O_2 \qquad (2)$$
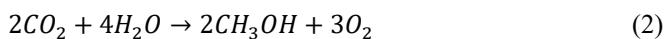
Following this equation, the reaction Gibbs free energy (ΔG) was predicted to be 638.73 kJ·mol^{-1} (or 6.62 eV per molecule).[42,43]

$$E_{CH_3OH} = \sum_i n_{photon,\ i} \times \frac{6 \times \text{numbers of generated } CH_3OH}{n_{photon,\ i}} \times \frac{1}{6} \times 6.62eV \times 1.602 \times 10^{-19} J\ eV^{-1} \quad (3)$$

$$E_{solar} = \sum_i n_{photon,\ i} \times \frac{hc}{\lambda_i} \qquad (4)$$

where $n_{photon,\ i}$ is the number of photons per interval I, with a wavelength of λ_i.

$$STF = \frac{\text{Methanol production rate } (mmol\ s^{-1}) \times 638730\ J\ mol^{-1}}{\text{Light intensity } (W\ cm^{-2}) \times \text{Wafer area } (cm^2)} \qquad (5)$$

The light intensity was calibrated with a Newport power meter light detector with 9 cm (distance from the device to the lamp lower end), shaded by aluminum foil with a 1 cm window to receive irradiance. Two wavelength filters (AM1.5G and 400nm long pass) were applied to simulate the visible light spectrum in solar light with intensity around 3 W·cm^{-2}. We note that the theoretical maximum efficiency for methanol generation is predicted to be 35.2%.[42]

Calculation of turnover number (TON) and turnover frequency (TOF). The TON for photocatalytic CO_2 reduction reaction

was calculated, as follows:

$$TON = \frac{Methanol\ production\ amount\ (mmol)}{photocatalyst\ amount\ (mmol)} \qquad (6)$$

$$TOF = \frac{Methanol\ production\ amount\ (mmol)}{photocatalyst\ amount\ (mmol) \times reaction\ time\ (hour)} \qquad (7)$$

The amount of metal catalysts ($Rh/Cu/Cr_2O_3$) used in the photocatalytic CO_2 reduction reaction was measured to be 0.29 μmol·cm^{-2} by AES-ICP test.

Computational Details. DFT calculations with periodic boundary conditions were performed using the Vienna Ab initio Simulation Package (VASP)[44-47] version 5.4. We used the Perdew-Burke-Ernzerhof (PBE)[48] exchange-correlation functional and the projected-augmented wave (PAW) method[49,50] to describe the ion-electron interactions. Spin-polarized Kohn-Sham calculations were performed to properly describe the localized 3d electrons of Cr. All calculations involving Fe atoms were performed with the spin polarized DFT+U method, using the rotational-invariant formalism developed by Dudarev *et al.*[51] The empirical parameter U_{eff} was chosen to be 4.0 eV for Cr 3d electrons, as used in the literature[52] for chromia. Dispersion interactions were considered using Grimme's empirical dispersion correction version 3 with Becke-Johnson damping (D3-BJ). The cutoff energy for the plane wave basis function is 450 eV. The Gaussian smearing method and a smearing parameter of σ = 0.1 eV were used to facilitate the SCF convergence. The SCF convergence criterion was set to be 10^{-6} eV per unit cell. In the calculation of bulk structures, we allowed both the unit cell size and shape, as well as the ionic positions, to be relaxed. The geometry convergence criterion was set to be an energy change less than 10^{-5} eV per unit cell between two consecutive calculations. A 9 × 9 × 9 Monckhorst-Pack (MP) type k-point grid[53] was used for the geometry optimization of GaN, Cu, Rh, and CrOOH bulk structures. The calculations of isolated small molecules (CO_2, H_2O, H_2, and CH_3OH) were performed with a supercell of 15.0 Å × 15.0 Å × 15.0 Å. The Gaussian smearing method with a σ value of 0.1 eV were used in the calculations. A 1 × 1 × 1 MP type k-point grid was used to sample the Brillouin zone and the SCF convergence criterion was set to be 10^{-5} eV per unit cell. The frequency analysis was performed to get the vibrational frequencies with VASP. A step size of 0.015 Bohr was used in finite difference calculations to obtain numerical hessians for frequency calculations. The calculated vibrational frequencies could be used to verify the nature of the stationary points and to get the thermal contribution to the free energy. We used the VASPKit package[54] to obtain the thermal correction to the free energy at 298.15 K and 101325 Pascal if not otherwise specified. However, we used 8390 Pascals, the saturated vapor pressure of H_2O at 298.15 K, to get the free energy contribution to $H_2O(l)$. To minimize the unphysical behavior caused by low frequency modes, the vibrational modes with frequencies lower than 50 cm^{-1} were replaced by 50 cm^{-1} as implemented in VASPKit. We constructed the slab models for the GaN(10-10), CrOOH(001), Cu(111), and Rh(111) facets. Based on the these slab models, we constructed GaN(100)/Rh(111), GaN(100)/Cu(111), Rh(111)/Cu(111), Rh(111)/CrOOH(001), Cu(111)/CrOOH(001) interfaces. The convergence criterion for geometries optimization was set to be -0.02 eV/Å.

Data Availability. Supporting data of this study are available within the paper. Further details regarding the data are available from the corresponding author upon reasonable request.

References

1. Zeng, X. J. *et al.* Single-Atom to Single-Atom Grafting of Pt-1 onto Fe-N-4 Center: Pt-1@Fe-N-C Multifunctional Electrocatalyst with Significantly Enhanced Properties. *Advanced Energy Materials* **8**, (2018).
2. De Luna, P. *et al.* What would it take for renewably powered electrosynthesis to displace petrochemical processes? *Science* **364**, eaav3506, (2019).
3. Zhang, B. & Sun, L. Artificial photosynthesis: opportunities and challenges of molecular catalysts. *Chemical Society Reviews* **48**, 2216-2264, (2019).
4. Mehla, S. *et al.* Porous crystalline frameworks for thermocatalytic CO_2 reduction: an emerging paradigm. *Energy Environ. Sci.* **14**, 320-352, (2021).
5. Zhang, W. *et al.* Progress and Perspective of Electrocatalytic CO_2 Reduction for Renewable Carbonaceous Fuels and Chemicals. *Advanced Science* **5**, 1700275, (2018).
6. Melchionna, M. & Fornasiero, P. Updates on the Roadmap for Photocatalysis. *ACS Catalysis* **10**, 5493-5501, (2020).
7. Li, X., Yu, J., Jaroniec, M. & Chen, X. Cocatalysts for Selective Photoreduction of CO_2 into Solar Fuels. *Chemical Reviews* **119**, 3962-4179, (2019).
8. Habisreutinger, S. N., Schmidt-Mende, L. & Stolarczyk, J. K. Photocatalytic Reduction of CO_2 on TiO_2 and Other Semiconductors. *Angew. Chem.-Int. Edit.* **52**, 7372-7408, (2013).
9. AlOtaibi, B., Fan, S., Wang, D., Ye, J. & Mi, Z. Wafer-Level Artificial Photosynthesis for CO_2 Reduction into CH_4 and CO Using GaN Nanowires. *ACS Catalysis* **5**, 5342-5348, (2015).
10. Hansen, H. A., Varley, J. B., Peterson, A. A. & Nørskov, J. K. Understanding Trends in the Electrocatalytic Activity of Metals and Enzymes for CO_2 Reduction to CO. *The Journal of Physical Chemistry Letters* **4**, 388-392, (2013).
11. Nitopi, S. *et al.* Progress and Perspectives of Electrochemical CO_2 Reduction on Copper in Aqueous Electrolyte. *Chemical Reviews* **119**, 7610-7672, (2019).
12. Graentzdoerffer, A., Rauh, D., Pich, A. & Andreesen, J. R. Molecular and biochemical characterization of two tungsten- and selenium-containing formate dehydrogenases from Eubacterium acidaminophilum that are associated with components of an iron-only hydrogenase. *Archives of microbiology* **179**, 116-130, (2003).
13. Reda, T., Plugge, C. M., Abram, N. J. & Hirst, J. Reversible interconversion of carbon dioxide and formate by an electroactive enzyme. **105**, 10654-10658, (2008).
14. Hartmann, T. & Leimkühler, S. The oxygen-tolerant and NAD+-dependent formate dehydrogenase from Rhodobacter capsulatus is able to catalyze the reduction of CO_2 to formate. *The FEBS journal* **280**, 6083-6096, (2013).
15. Schuchmann, K. & Müller, V. Direct and reversible hydrogenation of CO_2 to formate by a bacterial carbon dioxide reductase. *Science* **342**, 1382-1385, (2013).
16. Bassegoda, A., Madden, C., Wakerley, D. W., Reisner, E. & Hirst, J. Reversible Interconversion of CO_2 and Formate by a Molybdenum-Containing Formate Dehydrogenase. *Journal of the American Chemical Society* **136**, 15473-15476, (2014).

17. Maia, L. B., Fonseca, L., Moura, I. & Moura, J. J. G. Reduction of Carbon Dioxide by a Molybdenum-Containing Formate Dehydrogenase: A Kinetic and Mechanistic Study. *Journal of the American Chemical Society* **138**, 8834-8846, (2016).

18. Yu, X., Niks, D., Mulchandani, A. & Hille, R. Efficient reduction of CO(2) by the molybdenum-containing formate dehydrogenase from Cupriavidus necator (Ralstonia eutropha). *The Journal of biological chemistry* **292**, 16872-16879, (2017).

19. Sakai, K., Kitazumi, Y., Shirai, O., Takagi, K. & Kano, K. J. E. C. Direct electron transfer-type four-way bioelectrocatalysis of CO2/formate and NAD+/NADH redox couples by tungsten-containing formate dehydrogenase adsorbed on gold nanoparticle-embedded mesoporous carbon electrodes modified with 4-mercaptopyridine. **84**, 75-79, (2017).

20. Robinson, W. E., Bassegoda, A., Reisner, E. & Hirst, J. Oxidation-State-Dependent Binding Properties of the Active Site in a Mo-Containing Formate Dehydrogenase. *Journal of the American Chemical Society* **139**, 9927-9936, (2017).

21. Kibria, M. G. *et al.* Visible light-driven efficient overall water splitting using p-type metal-nitride nanowire arrays. *Nature Communications* **6**, 6797, (2015).

22. Kibria, M. G. *et al.* One-Step Overall Water Splitting under Visible Light Using Multiband InGaN/GaN Nanowire Heterostructures. *ACS Nano* **7**, 7886-7893, (2013).

23. Wang, D. *et al.* Wafer-Level Photocatalytic Water Splitting on GaN Nanowire Arrays Grown by Molecular Beam Epitaxy. *Nano Letters* **11**, 2353-2357, (2011).

24. Schouten, K. J. P., Kwon, Y., van der Ham, C. J. M., Qin, Z. & Koper, M. T. M. A new mechanism for the selectivity to C1 and C2 species in the electrochemical reduction of carbon dioxide on copper electrodes. *Chemical Science* **2**, 1902-1909, (2011).

25. Kuhl, K. P., Cave, E. R., Abram, D. N. & Jaramillo, T. F. New insights into the electrochemical reduction of carbon dioxide on metallic copper surfaces. *Energy Environ. Sci.* **5**, 7050-7059, (2012).

26. Peterson, A. A., Abild-Pedersen, F., Studt, F., Rossmeisl, J. & Nørskov, J. K. How copper catalyzes the electroreduction of carbon dioxide into hydrocarbon fuels. *Energy Environ. Sci.* **3**, 1311-1315, (2010).

27. Reske, R., Mistry, H., Behafarid, F., Roldan Cuenya, B. & Strasser, P. Particle Size Effects in the Catalytic Electroreduction of CO2 on Cu Nanoparticles. *Journal of the American Chemical Society* **136**, 6978-6986, (2014).

28. Li, Y. *et al.* Structure-Sensitive CO2 Electroreduction to Hydrocarbons on Ultrathin 5-fold Twinned Copper Nanowires. *Nano Letters* **17**, 1312-1317, (2017).

29. Zhang, S.-Y., Zhu, H.-L. & Zheng, Y.-Q. Surface modification of CuO nanoflake with Co3O4 nanowire for oxygen evolution reaction and electrocatalytic reduction of CO2 in water to syngas. *Electrochimica Acta* **299**, 281-288, (2019).

30. Li, C. W., Ciston, J. & Kanan, M. W. Electroreduction of carbon monoxide to liquid fuel on oxide-derived nanocrystalline copper. *Nature* **508**, 504-507, (2014).

31. Zhou, B. *et al.* Highly efficient binary copper−iron catalyst for photoelectrochemical carbon dioxide reduction toward methane. **117**, 1330-1338, (2020).

32. Wu, Y. A. *et al.* Facet-dependent active sites of a single Cu2O particle photocatalyst for CO2 reduction to methanol. *Nature Energy* **4**, 957-968, (2019).

33. Yoshida, M. *et al.* Role and Function of Noble-Metal/Cr-Layer Core/Shell Structure Cocatalysts for Photocatalytic Overall Water Splitting Studied by Model Electrodes. *The Journal of Physical Chemistry C* **113**, 10151-10157, (2009).

34. Zhu, S., Li, T., Cai, W.-B. & Shao, M. CO2 Electrochemical Reduction As Probed through Infrared Spectroscopy. *ACS Energy Letters* **4**, 682-689, (2019).

35. Wang, W. *et al.* Photocatalytic C–C Coupling from Carbon Dioxide Reduction on Copper Oxide with Mixed-Valence Copper(I)/Copper(II). *Journal of the American Chemical Society* **143**, 2984-2993, (2021).

36. Tang, Q.-L., Hong, Q.-J. & Liu, Z.-P. CO2 fixation into methanol at Cu/ZrO2 interface from first principles kinetic Monte Carlo. *Journal of Catalysis* **263**, 114-122, (2009).

37. Grabow, L. C. & Mavrikakis, M. Mechanism of Methanol Synthesis on Cu through CO2 and CO Hydrogenation. *ACS Catalysis* **1**, 365-384, (2011).

38. Pavlišič, A., Huš, M., Prašnikar, A. & Likozar, B. Multiscale modelling of CO2 reduction to methanol over industrial Cu/ZnO/Al2O3 heterogeneous catalyst: Linking ab initio surface reaction kinetics with reactor fluid dynamics. *Journal of Cleaner Production* **275**, 122958, (2020).

39. Appel, A. M. *et al.* Frontiers, Opportunities, and Challenges in Biochemical and Chemical Catalysis of CO$_2$ Fixation. *Chemical Reviews* **113**, 6621-6658, (2013).

40. Boyington, J. C., Gladyshev, V. N., Khangulov, S. V., Stadtman, T. C. & Sun, P. D. Crystal Structure of Formate Dehydrogenase H: Catalysis Involving Mo, Molybdopterin, Selenocysteine, and an Fe$_4$S$_4$ Cluster. **275**, 1305-1308, (1997).

41. Yang, K. R., Lakshmi, K. V., Brudvig, G. W. & Batista, V. S. Is Deprotonation of the Oxygen-Evolving Complex of Photosystem II during the S1 → S2 Transition Suppressed by Proton Quantum Delocalization? *Journal of the American Chemical Society* **143**, 8324-8332, (2021).

42. Singh, M. R., Clark, E. L. & Bell, A. T. Thermodynamic and achievable efficiencies for solar-driven electrochemical reduction of carbon dioxide to transportation fuels. **112**, E6111-E6118, (2015).

43. Adelmann, C. *et al.* Self-assembled InGaN quantum dots grown by molecular-beam epitaxy. **76**, 1570-1572, (2000).

44. Kresse, G. & Hafner, J. Ab initio molecular dynamics for liquid metals. *Phys. Rev. B* **47**, 558-561, (1993).

45. Kresse, G. & Hafner, J. Ab initio molecular-dynamics simulation of the liquid-metal–amorphous-semiconductor transition in germanium. *Phys. Rev. B* **49**, 14251-14269, (1994).

46. Kresse, G. & Furthmüller, J. Efficiency of ab-initio total energy calculations for metals and semiconductors using a plane-wave basis set. *Comput. Mater. Sci.* **6**, 15-50, (1996).

47. Kresse, G. & Furthmüller, J. Efficient iterative schemes for ab initio total-energy calculations using a plane-wave basis set. *Phys. Rev. B* **54**, 11169-11186, (1996).

48. Perdew, J. P., Burke, K. & Ernzerhof, M. Generalized gradient approximation made simple. *Phys. Rev. Lett.* **77**, 3865-3868, (1996).

49. Blöchl, P. E. Projector augmented-wave method. *Phys. Rev. B* **50**, 17953-17979, (1994).

50. Kresse, G. & Joubert, D. From ultrasoft pseudopotentials to the projector augmented-wave method. *Phys. Rev. B* **59**, 1758-1775, (1999).

51. Dudarev, S. L., Botton, G. A., Savrasov, S. Y., Humphreys, C. J. & Sutton, A. P. Electron-energy-loss spectra and the structural stability of nickel oxide: An LSDA+*U* study. *Phys. Rev. B* **57**, 1505-1509, (1998).

52. Wang, L., Maxisch, T. & Ceder, G. Oxidation energies of transition metal oxides within the GGA+*U* framework. *Phys. Rev. B* **73**, 195107, (2006).

53. Monkhorst, H. J. & Pack, J. D. Special points for Brillouin-zone integrations. *Phys. Rev. B* **13**, 5188-5192, (1976).

54. Wang, V., Xu, N., Liu, J.-C., Tang, G. & Geng, W. T. VASPKIT: A pre- and post-processing program for VASP code. *arXiv:1908.08269 (2019), https://arxiv.org/abs/1908.08269*.
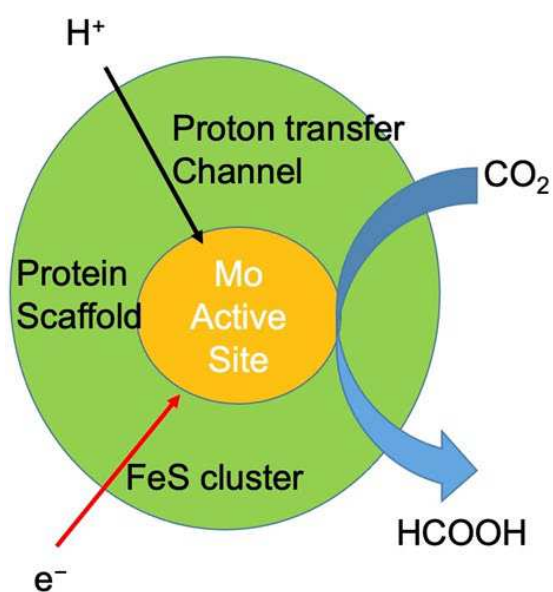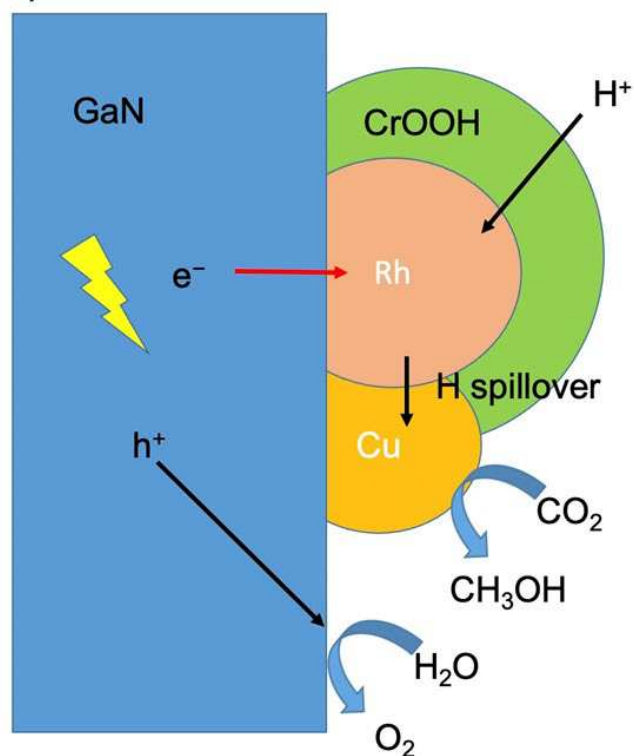
Scheme 1. Design principle of a photochemical architecture for artificial photosynthesis of methanol from carbon dioxide and water. a) Vectorial proton and electron transfer in liquid products dehydrogenase and **b)** Rh/Cu/CrOOH@InGaN for highly selective of CO_2 reduction toward CH_3OH.
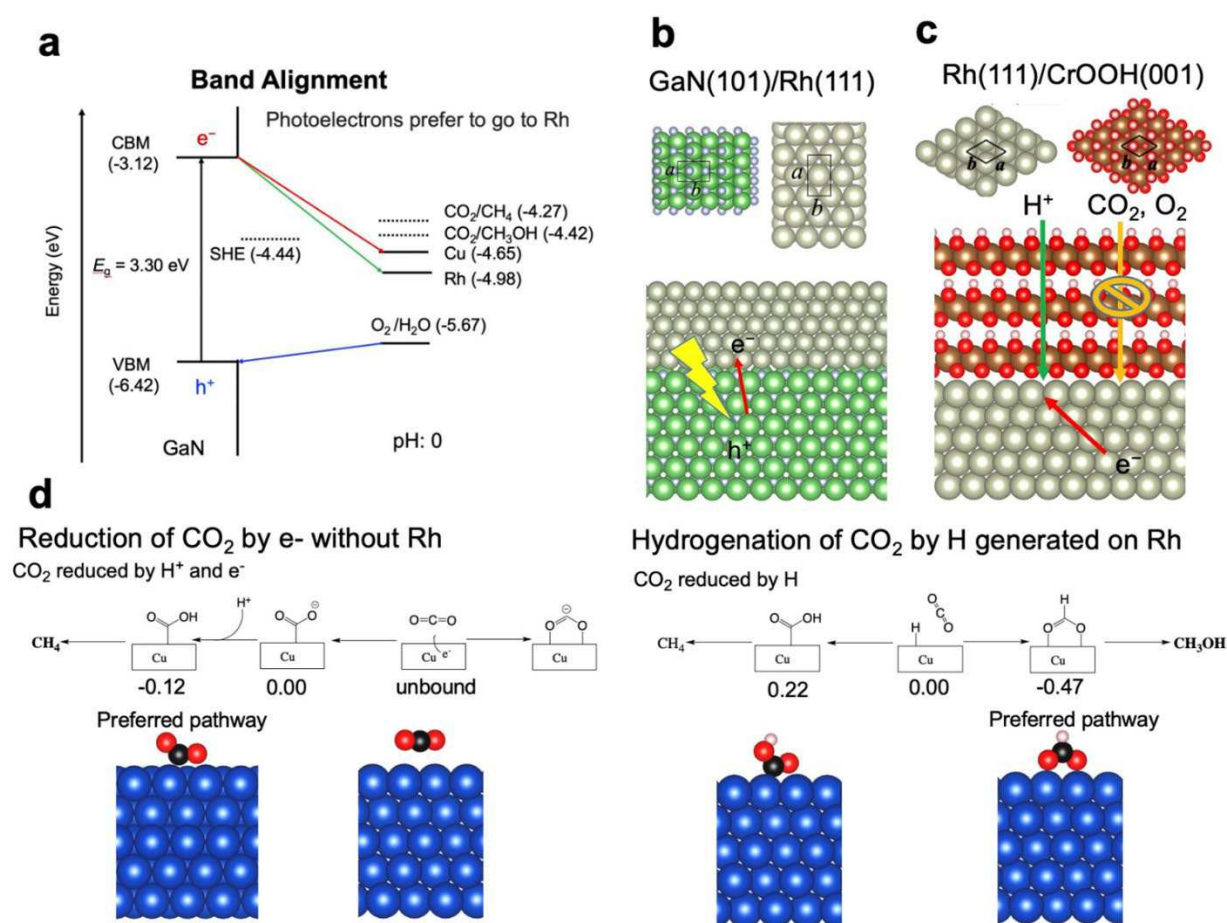
Figure 1. **Design principle and predicted selectivity of CO₂ reduction. a**) band alignment of the conduction and valence bands of GaN, work functions of Cu and Rh, and absolute redox potentials; **b**) GaN(101) and Rh(111) interface; **c**) Rh(111) and CrOOH (001) interface; **d**) Preferred pathways of CO₂ reduction by surface H atoms and e⁻ and H⁺ on the Cu(111) surface (relative energies in the unit of eV using $H_2 + CO_2$ and bare Cu surfaces as the zero-reference). White, black, light blue, red, green, brown, blue, and grey spheres represent H, C, N, O, Ga, Cr, Cu, and Rh atoms, respectively.
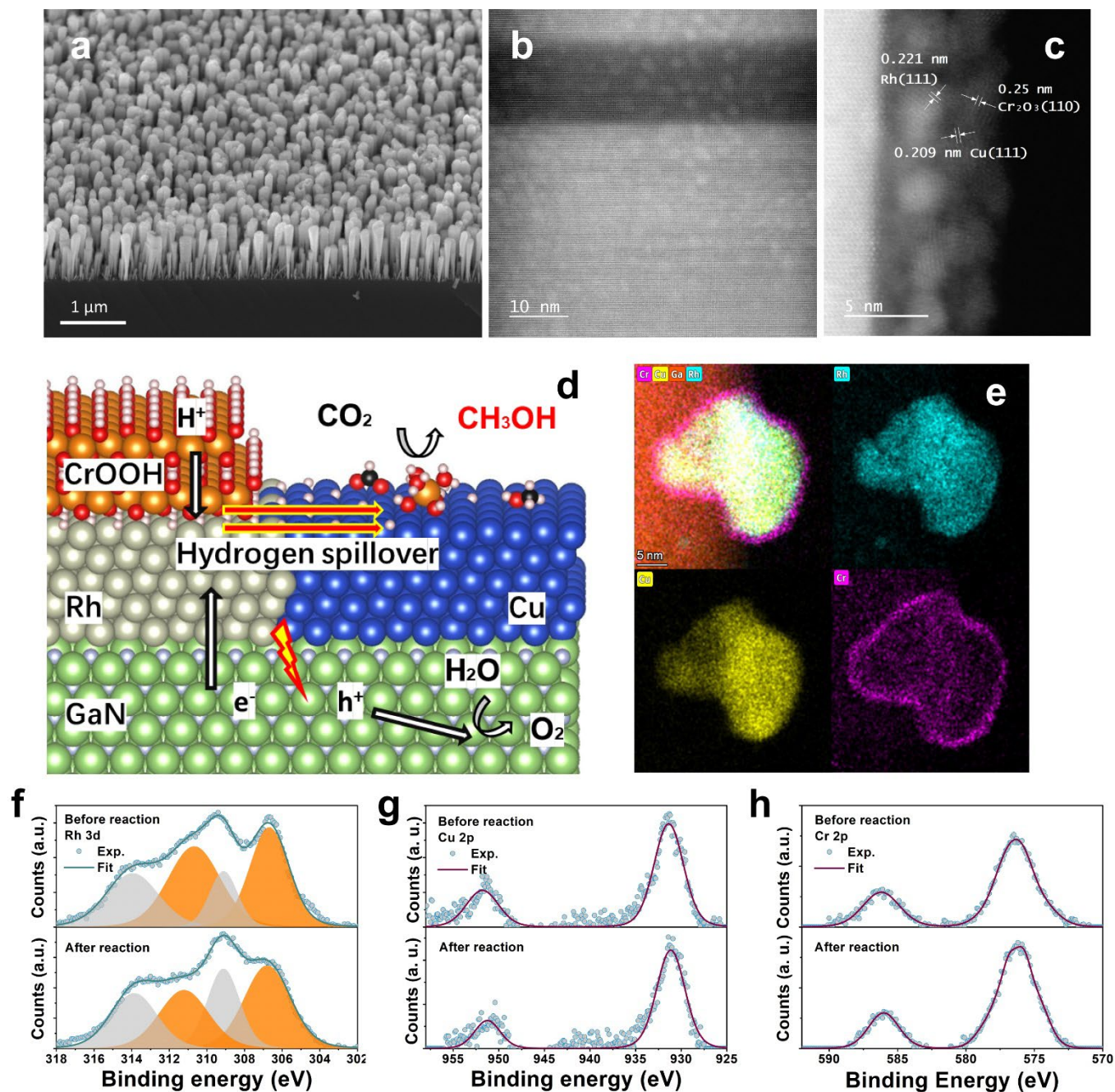
Figure 2. Synthesis and characterization of Rh/Cu/CrOOH@GaInN photocatalysts. a) 45° tilted-SEM image of GaInN nanowires grown on Si wafer after photo deposition of Rh, Cr, and Cu co-catalysts; **b), c)** HAADF-STEM image; **d)** Schematic illustration of the reaction mechanism, including charge carrier generation upon photon excitation of GaInN, electron migration to Rh, hydrogen spillover from Rh to Cu, and CO_2 reduction to CH_3OH on Cu surface. **e), f), g), h),** Elemental mapping images of Rh/Cu/CrOOH@GaInN. Ga, green; N, silver; Cu, blue; Rh, beige; Cr, orange; O, red; C, black; and H, white. High-resolution XPS spectra of Rh 3d, **i)**, Cu 2p, **j)** and Cr 2p, **k)** loaded on GaInN nanowire arrays before (upper panel) and after (lower panel) photocatalysis reaction. The grey symbols and curves represent the original data and fitting results of Rh 3d, Cu 2p and Cr 2p, respectively. Shown in **i)**, the orange area represents the metal state of the rhodium while the grey area represents the oxygen adsorption on rhodium surface. a. u. denotes arbitrary units.
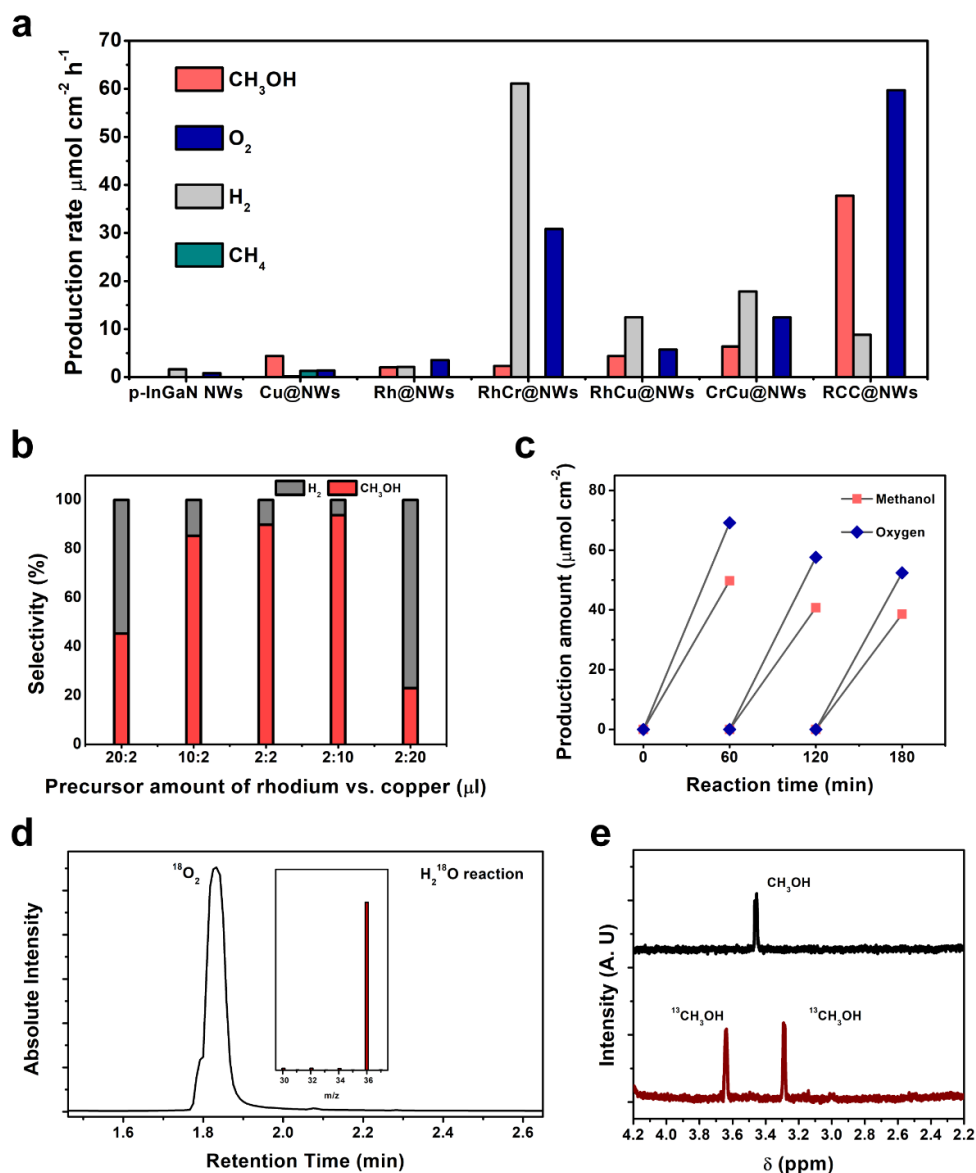
Figure 3. Photocatalytic performance of Rh/Cu/CrOOH@GaInN. **a)** Production rates of CH_3OH, CH_4, H_2, and O_2 on (from left to right) GaInN nanowires, Cu/GaInN, Rh/GaInN, RhCr/GaInN, RhCu/GaInN, CrCu/GaInN, and RhRuCr/GaInN. **b)** Variations of methanol selectivity (left axis) vs. co-catalyst deposition conditions. The production rates of methanol and hydrogen are shown in the right axis. Here 20:2 means 20μL of Rh precursor and 2μL Cu precursor were used in the photoadaptation process. **c)** Methanol production under optimized co-catalyst conditions during twelve cycles of measurements. Each cycle lasted for one hour. After each cycle, the solution was removed and refilled, and the sample was taken out of the reaction chamber and rinsed by deionized water to remove the potentially attached methanol molecules. Experimental conditions: 50 mL deionized water, CO_2, 300 W Xenon-lamp, 3.5 W/cm^2, AM1.5G + 400nm long pass filter. **d)** GC-MS spectrum of 18-oxygen generated during the CO_2 reduction reaction with 18-O labelled water. **e)** NMR H-spectrum of ^{12}C methanol generated during the CO_2 reduction reaction with CO_2. NMR H-spectrum of ^{13}C methanol generated during the CO_2 reduction reaction with 13-C labelled CO_2.
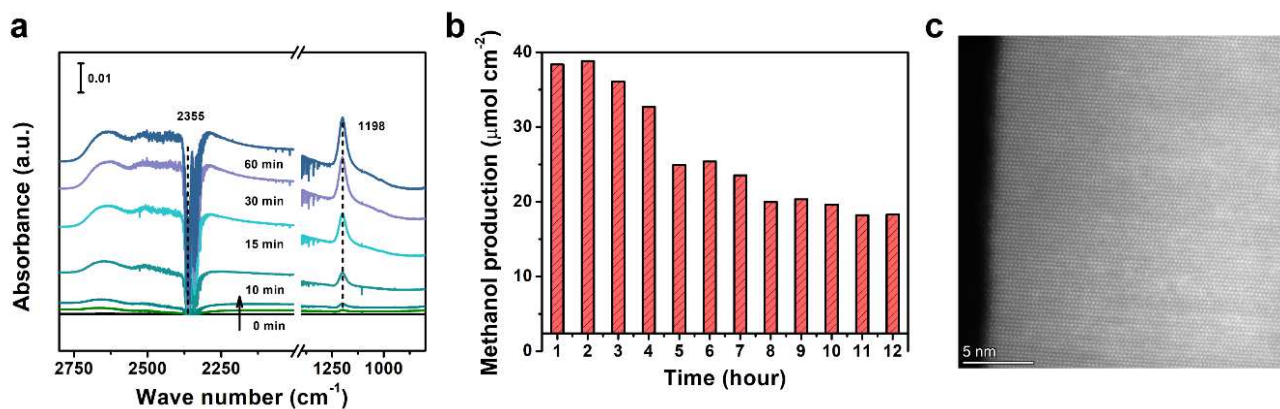
Figure 4. Long-term stability performance of Rh/Cu/CrOOH@GaInN photocatalysts. a) ATR spectrum collected from $CO_2/H_2O/Ga(In)N$ nanowires interface under 420nm (3W, LED) light illumination in 60min using RCC cocatalysts. **b)** Stability tests up to 12 cycles, 720 minutes. Each cycle lasted for one hour. After each cycle, the solution was removed and refiled, and the sample was taken out of the reaction chamber and rinsed by deionized water to remove the potentially attached methanol molecules. **c)** STEM image of $RhCuCr_2O_3@GaInN/GaN$ nanowires sample after 12 cycles reaction. Most particles were removed but the nanowire rod was well preserved.
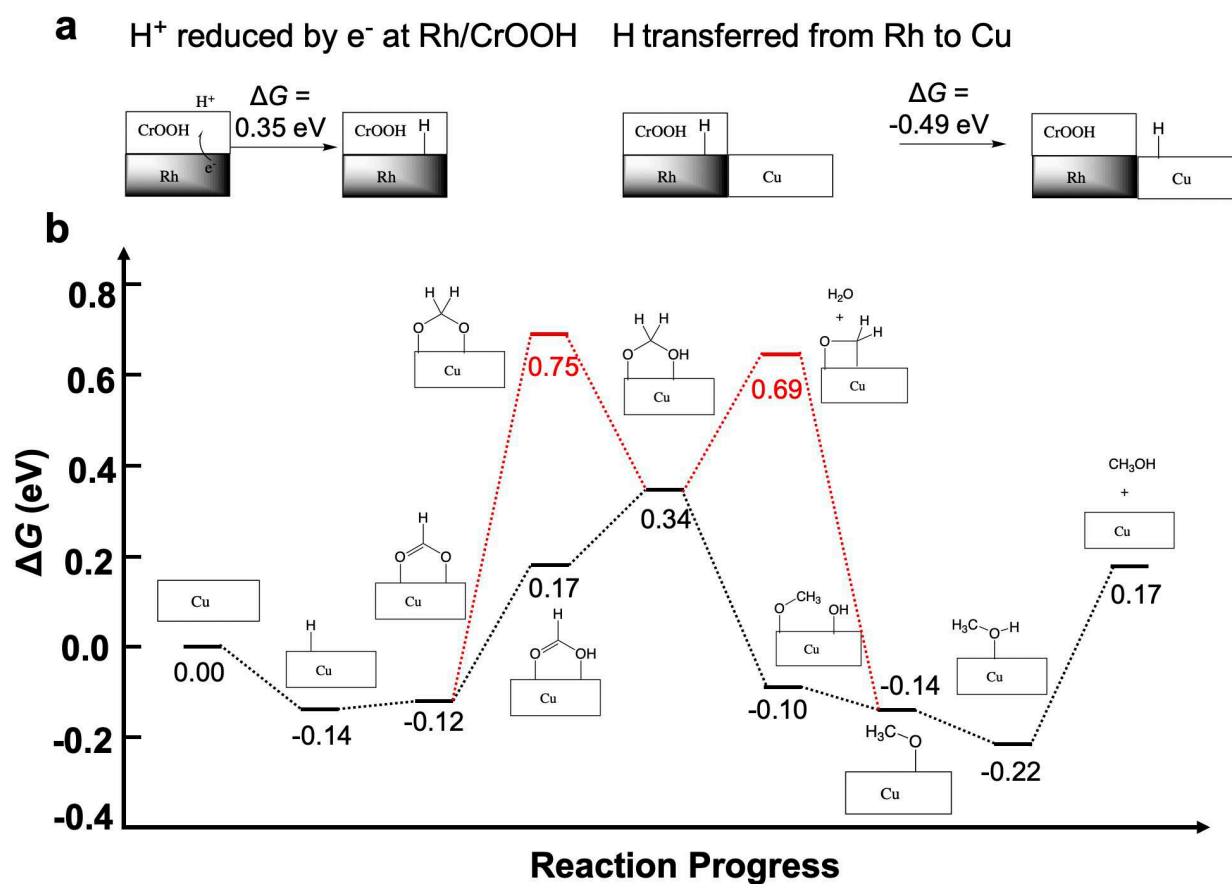
Figure 5. Mechanism of CO₂ reduction by H on Cu to produce CH₃OH. a) Schematic representation of proton reduction at the Rh/CrOOH interface and hydrogen spillover from Rh/CrOOH interface to Cu surface; **b**) Free energy profile of CO_2 reduction by surface hydrogen atoms toward CH_3OH at 298.15 K. The relative free energy changes are calculated using CO_2, H_2, and the Cu(111) surface as the zero reference.
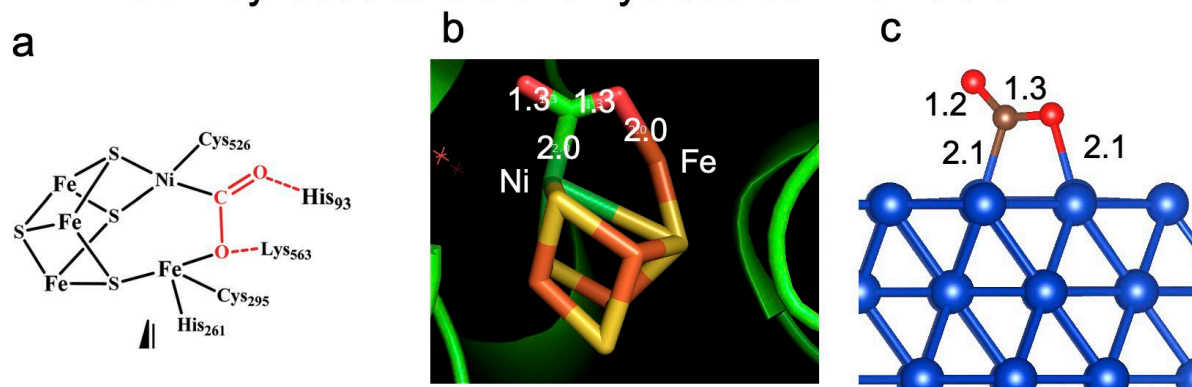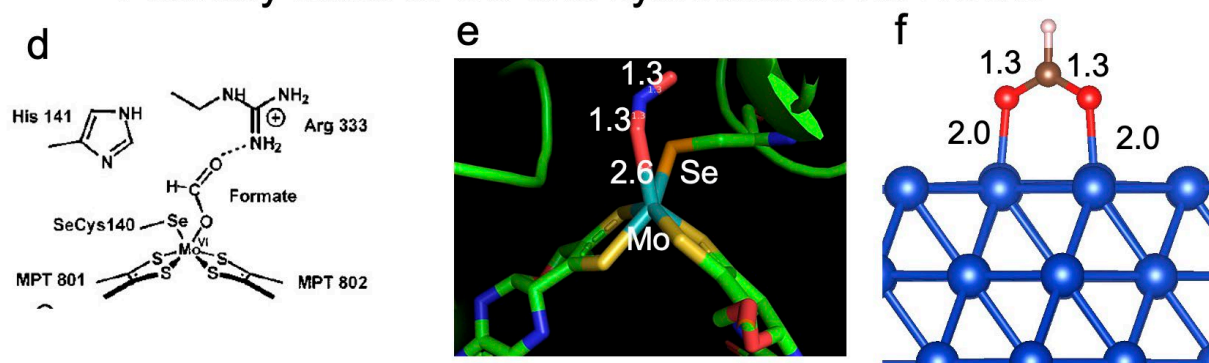
Figure 6. Comparison of two pathways of CO₂ reduction in natural enzymes and Cu surfaces. (a) proposed binding mode of CO_2 at the active site of the CO dehydrogenase; (b) Crystal structure of CO_2 biding at the Ni, Fe cluster in the CO dehydrogenation (PDB ID: 3b52); (c) optimized structure of CO_2 binding to the negative charge Cu surface; (d) proposed binding mode of CO_2 at the active site of the formate dehydrogenase; (b) Crystal structure of NO_2^- biding at the Mo cluster in the formate dehydrogenation (PDB ID: 1dfi); (c) optimized structure of CO_2 binding to surface bound H atom on Cu surface.

Supplementary Files

This is a list of supplementary files associated with this preprint. Click to download.

- SupplementaryInformation.pdf